Extreme Mechanics Letters 13 (2017) 116–125

Contents lists available at ScienceDirect

Extreme Mechanics Letters

journal homepage: www.elsevier.com/locate/eml

Role of nonlinear elasticity in mechanical impedance tuning of annular dielectric elastomer membranes

A. Cugno [a,b], S. Palumbo [a], L. Deseri [a,d,e,f,g], M. Fraldi [b,c], C. Majidi [f,h,*]

[a] Civil, Environmental & Mechanical Engineering, University of Trento, 38123 Trento, Italy
[b] Structures for Engineering and Architecture, University of Napoli Federico II, 80125 Napoli, Italy
[c] Interdisciplinary Research Center for Biomaterials, University of Napoli Federico II, 80125 Napoli, Italy
[d] Mechanical & Materials Science, University of Pittsburgh, Pittsburgh, PA 15261, USA
[e] Mechanical, Aerospace & Civil Engineering, Brunel University London, Uxbridge, UB8 3PH, UK
[f] Mechanical Engineering, Carnegie Mellon University, Pittsburgh, PA 15213, USA
[g] Nanomedicine, The Methodist Hospital Research Institute, MS B-490, Houston, TX 77030, USA
[h] Civil & Environmental Engineering, Carnegie Mellon University, Pittsburgh, 15213 PA, USA

ARTICLE INFO

Article history:
Received 18 November 2016
Available online 6 March 2017

Keywords:
Dielectric elastomer
Membrane theory
Nonlinear elasticity
Aerospace structures

ABSTRACT

We use finite elasticity to examine the behavior of a lightweight mechanism for rapid, reversible, and low-power control of mechanical impedance. The device is composed of a central shaft suspended by an annular membrane of prestretched dielectric elastomer (DE), which is coated on both sides with a conductive film. Applying an electrical field across the thickness of the membrane, attractive Coulombic forces (so-called "Maxwell stresses") are induced that (i) squeeze the annulus, (ii) relieve the membrane stress, and (iii) reduce the mechanical resistance of the elastomer to *out-of-plane* deflection. This variable stiffness architecture was previously proposed by researchers who performed an experimental implementation and demonstrated a 10× change in stiffness. In this manuscript, we generalize this approach to applications in aerospace and robotics by presenting a complete theoretical analysis that establishes a relationship between mechanical impedance, applied electrical field, device geometry, and the constitutive properties of the dielectric elastomer. In particular, we find that the stiffness reduction under applied voltage is non-linear. Such decay is most significant when the Maxwell stress is comparable to the membrane prestress. For this reason, both the prestretch level and the hyperelastic properties of the DE membrane have a critical influence on the impedance response.

1. Introduction

In current aerospace applications, active mechanical impedance control typically requires clutches, brakes, transmissions, and other hardware that depend on motors and hydraulics. While adequate for large conventional systems, these variable stiffness mechanisms may be challenging to implement in smaller, collapsible, or structurally reconfigurable systems that require continuous stiffness change or complex triggering. For these emerging applications, rigidity-tuning hardware should be replaced with thin, lightweight, elastic materials and composites that are capable of modulating their stiffness through direct electrical operation. Potential approaches include electrostatic activation of electro-active polymers (EAPs) and electrical (Joule) heating of thermally-responsive materials. The latter has been demonstrated with phase-change of low-melting point metal alloys [1,2], glass transition of shape memory polymer [1,3,4], and softening of conductive thermoplastic elastomers [5]. While promising for applications that involve only intermittent operation, thermally-activated rigidity tuning is typically too slow (∼0.01–1 Hz) and energetically costly (∼0.1–10 W) for dynamical systems that require high cycling rates. Instead, recent efforts in aerospace and space research have focused on EAPs that couple shape and stiffness with rapid and low-power electrostatic activation [6–8].

Here, we use finite elasticity to examine a particularly promising class of EAP architectures that can be used for robust mechanical impedance control. Referring to Fig. 1, the structure is composed of a central shaft (or "shuttle") that is suspended by an annular membrane of prestretched dielectric elastomer (DE).

* Corresponding author.
E-mail address: cmajidi@andrew.cmu.edu (C. Majidi).

http://dx.doi.org/10.1016/j.eml.2017.03.001
2352-4316/

Both sides of the DE film are coated with a conductive fluid (e.g. liquid metal alloy), grease (silicone oil mixed with carbon powder), or elastomer (silicone rubber mixed with carbon powder) that remains conductive as the DE film is stretched. Connecting the film to a power supply and applying a voltage drop Φ across the thickness induces a Coulombic attraction, sometimes referred to as "Maxwell stress", that squeezes the membrane and relieves its prestretch. This stress reduction results in the lowering of the mechanical resistance of the shuttle to deformations in the out-of-plane direction.

The idea of a variable-stiffness device with EAPs was first introduced by Pelrine, Kornbluh, et al. [9,10]. They performed experimental tests to show the effect of the voltage on the stiffness of a framed prestretched planar acrylic film, obtaining a reduction of the stiffness up to 10× under an applied voltage drop of 6 kV. Variable stiffness with DE membranes has also been proposed by Carpi et al. [11], who explore applications in hand rehabilitation. The design examined in this study (Fig. 1) was first proposed for voltage-controlled stiffness tuning by Dastoor & Cutkosky [12]. Their implementation showed a 7–10× reduction in stiffness and exhibited electromechanical coupling that was consistent with theoretical predictions based on a linearized model. While inadequate for modeling large strains or electromechanical instabilities [13], the linear theory enabled the authors to identify the important role of elastomer stiffness and prestretch in the coupling between applied voltage and mechanical impedance. Building on this work, Orita and Cutkosky [14] tested a multi-layer diaphragm device and performed a nonlinear FEA study with the aim of identifying sources of failure and approaches for failure mitigation. The design in Fig. 1 has also been employed for replicating human pulse signal by means of a model-based robust control [15]. For applications in acoustics, Lu et al. [16] use voltage-controlled stiffness tuning to alter the resonance peaks of a membrane-based silencer. Applying different external voltages enabled a maximum resonance frequency shift of 59.5 Hz and allowed the silencer to adjust its absorption of target noise without any addition of mechanical part. Related analysis by [17] shows that the sound transmission band-gap of the membrane filter can be tuned by adjusting the voltage applied to the membrane.

In addition to the analyses in [12] and [14], the mechanics of the annular DE membrane have been examined by He et al. [18]. They treated the membrane as a Neo-Hookean solid and found numerical solutions to the governing balance equations, which included the Maxwell stress associated with Φ. More recently, Melnikov and Ogden [19] performed a theoretically analysis on a related system composed of a tubular DE shell subject to a combination of (radial) electric field, internal air pressure, and axial mechanical loading. They used a nonlinear theory of electroelasticity that allowed them to predict a *loss of tension* associated with variations in electrical field.

In order to understand the underlying mechanics of the system originally presented by Dastoor [12] and draw practical insights for future aerospace applications, we must perform a more complete electromechanical analysis. As described in the following section (Section 2), the theory incorporates the kinematics of finite deformation, the nonlinear constitutive properties of a hyperelastic solid, and the electrical enthalpy induced by voltage-controlled electrostatic field. Analysis is performed by treating the DE film as a hyperelastic membrane and using variational techniques to determine the electro-elastostatic configuration that minimizes the potential energy. This approach is adapted from the methods presented in [20] for examining the axisymmetric deformation of an annular membrane [21] and builds on the field equations for DE actuators and transducers previously presented in [22–27]. Here, the dielectric is treated as either a Neo-Hookean or (two-parameter) Ogden solid, although the theory can be generalized to any constitutive law for an incompressible hyperelastic material.

In order to obtain an algebraic relationship between the stiffness and the applied voltage, we perform a linear incremental analysis with respect to (w.r.t.) the prestretched configuration. Both the numerical results of the nonlinear model and the linearized approximation suggest an electromechanical coupling that is consistent with the previous experimental observations [12]. We review these in Section 3 and discuss in Section 4 how the theory leads to new insights about the influence of the prestretch and applied voltage on mechanical response.

2. The electro-mechanical model

As shown in Fig. 1, the device is composed of an outer rigid frame with inner circular opening of radius R_e that is attached to a cylindrical bar of radius R_i through a prestretched annular DE membrane. Prior to stretching, the membrane has an inner radius R_i, outer radius $R_o = R_e/\lambda_p$ and thickness H. The membrane stress is controlled by applying a drop voltage Φ across compliant electrodes coated to the surfaces of the dielectric film. Such electromechanical coupling arises from the Maxwell stress tensor that is generated by the internal electrostatic field. As for any elastic film in tension, this change in membrane stress will lead to a change in the mechanical resistance to out-of-plane (*z-axis*) deflection.

2.1. Kinematics

Referring to Fig. 1, the current (deformed) configuration Ω can be obtained from a deformation mapping $\chi = \chi_0 \circ \chi_p$ that is composed as follows: (i) a uniform biaxial (pre)stretch $\mathbf{x}_p = \chi_p(\mathbf{X})$, which maps the body from the *reference configuration* Ω_0 to the *intermediate* one Ω_p, and (ii) a vertical deflection $\mathbf{x} = \chi_0(\mathbf{x}_p)$ induced by the prescribed shaft displacement $\bar{\mathbf{u}}$, which maps the body to Ω. For convenience, three different coordinate systems (COOS) and orthonormal bases are used to represent points in the body:

1. Cylindrical COOS in Ω_0, which describes material points in the reference stress-free configuration, spanned by the triad $\{\mathbf{E_s}, \mathbf{E}_\theta, \mathbf{E_3}\}$,
2. Cylindrical COOS in Ω_p with bases $\{\mathbf{e_s}, \mathbf{e}_\theta, \mathbf{e_3}\}$,
3. Curvilinear COOS in Ω with covariant bases $\{\mathbf{e_l}, \mathbf{e}_t, \mathbf{e_n}\}$ that are tangent to the coordinate lines.

The deformation gradient of the mapping χ can be multiplicatively decomposed as $\mathbf{F} = \mathbf{F}_0\mathbf{F}_p$. Here, $\mathbf{F}_p = \mathrm{diag}\{\lambda_p, \lambda_p, \lambda_p^{-2}\}$ is the deformation gradient due to the prestretch while $\mathbf{F}_0$ corresponds to the out-of-plane deflection. The transverse stretch λ_p^{-2} is obtained by the incompressibility constraint $\det \mathbf{F}_p = 1$ and gives the intermediate membrane thickness $h_p = H/\lambda_p^2$.

The deformation mapping $\mathbf{x} = \chi_0(\mathbf{x}_p)$, adapted from the membrane theory previously presented in [20], has the following form:

$$\chi_0(\mathbf{x}_p) = \mathbf{x}_p - x_3\mathbf{e}_3 + \mathbf{u}_0 + (x_3 + q)\,\mathbf{e}_n, \tag{1}$$

where $\mathbf{u_0} = \mathbf{u}_0(s,\theta)$ is the displacement of a point with coordinates (s,θ) on the midplane (for which $x_3 = 0$), $\mathbf{e}_n$ is the unit vector normal to the deformed surface, and $q(s,\theta,x_3)$ is the normal component of the displacement of points away from the midplane related to the deformed configuration. By definition, the function q (and its partial derivatives w.r.t. s and θ) must vanish on the midplane:

$$q(x_3 = 0) = \frac{\partial q}{\partial s}\Big|_{x_3=0} = \frac{1}{s}\frac{\partial q}{\partial \theta}\Big|_{x_3=0} = 0. \tag{2}$$

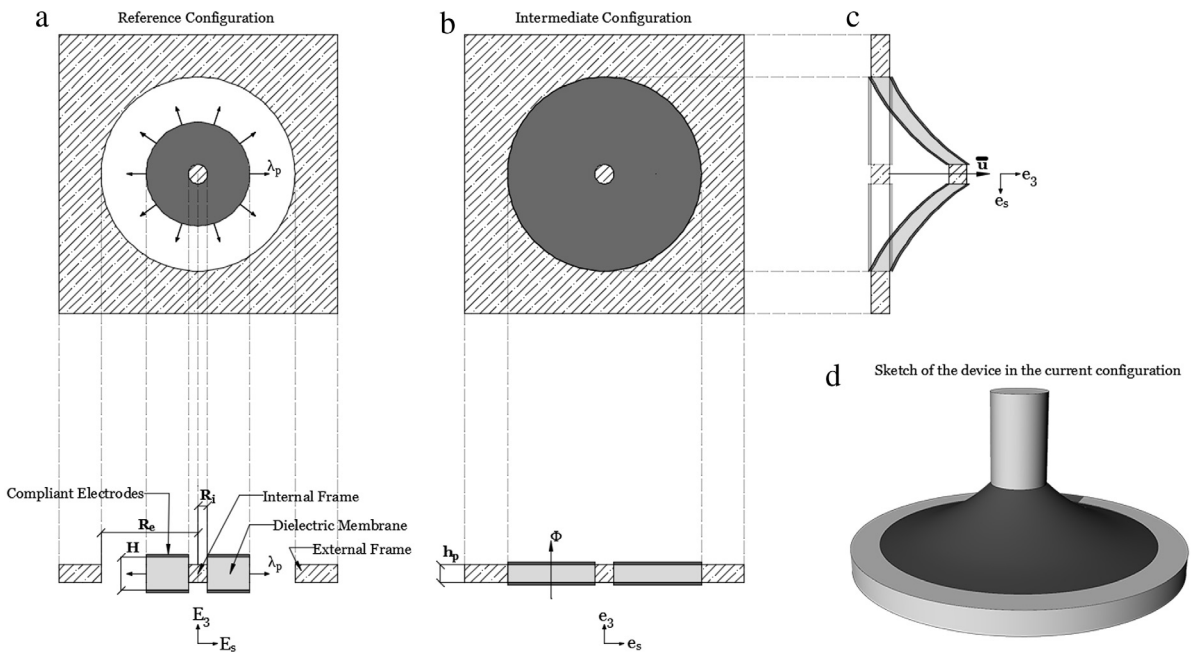

Fig. 1. Sketch of the diaphragm device in which an outer rigid frame with inner circular opening of radius R_e is attached to a cylindrical bar of radius R_i through a prestretched (λ_p) annular DE membrane with initial thickness H and prestretched thickness $h_p = H/\lambda_p^2$. In the membrane it is possible to induce a drop voltage Φ by means of two compliant electrodes. (a) Reference configuration, top view above and lateral view in the bottom; (b) Intermediate configuration, top view above and lateral view in the bottom; (c) Lateral view of the current configuration characterized by a prescribed pulling out displacement $\bar{u}$; (d) Sketch of the device in the current configuration.

The covariant bases at a point on a surface parallel to the midplane in the current configuration may be expressed as

$$\mathbf{e}_s' = \mathbf{e}_s + \frac{\partial}{\partial s}\mathbf{u}_0, \qquad \mathbf{e}_\theta' = \mathbf{e}_\theta + \frac{1}{s}\frac{\partial}{\partial \theta}\mathbf{u}_0$$
$$\text{and} \quad \mathbf{e}_n = \frac{\mathbf{e}_s' \times \mathbf{e}_\theta'}{\|\mathbf{e}_s' \times \mathbf{e}_\theta'\|}. \tag{3}$$

Noting that, for the membrane in the prestretched configuration, h_p becomes small w.r.t. the annular width, the deformation gradient $\mathbf{F}_0$ can be assumed homogeneous along the thickness and thus approximated as follows [20]:

$$\mathbf{F}_0 \simeq (\mathbf{F}_0)_{x_3=0} = \mathbf{I} - \mathbf{e}_3 \otimes \mathbf{e}_3 + \nabla \mathbf{u}_0 + \lambda_{n3}\mathbf{e}_n \otimes \mathbf{e}_3, \tag{4}$$

where $\lambda_{n3} = (1 + \partial q/\partial x_3)$ is hence independent from x_3. Because we are interested in the response of the device to a normal displacement imposed on the internal frame (see Fig. 1), we consider the deformation as axisymmetric. The resulting displacement $\mathbf{u_0}$ is then a function of the coordinate s and no displacement occurs in the θ direction:

$$\mathbf{u_0} = u_s(s)\mathbf{e}_s + u_3(s)\mathbf{e}_3 \quad \text{and} \quad q = q(s). \tag{5}$$

Substituting the expressions for $\mathbf{F}_p$ and $\mathbf{F}_0$ into $\mathbf{F}$, it is possible to write the right Cauchy–Green deformation tensor [28] as follows:

$$\mathbf{C} = \mathbf{F}^{\mathbf{T}}\mathbf{F} = \text{diag}\left\{\lambda_p^2\left[(u_s' + 1)^2 + (u_3')^2\right], \frac{\lambda_p^2 (u_s + s)^2}{s^2}, \frac{\lambda_{n3}^2}{\lambda_p^4}\right\}, \tag{6}$$

where the principal stretches are simply the square roots of the diagonal elements. Applying the incompressibility constraint yields the following expression for λ_{n3}:

$$\lambda_{n3} = \frac{s}{(u_s + s)\sqrt{(u_s' + 1)^2 + (u_3')^2}}. \tag{7}$$

2.2. Constitutive relations

To capture the nonlinear mechanics of the membrane, we treat it as an incompressible Ogden solid with two elastic coefficients. The constitutive relationship between the Cauchy stress and the principle stretches can be obtained from the strain energy density function Ψ. For a selected pair of exponents, Ψ has the form [29]:

$$\Psi = \frac{1}{2}\mu_1\left(\lambda_s^2 + \lambda_\theta^2 + \lambda_3^2 - 3\right) + \frac{1}{4}\mu_2\left(\lambda_s^4 + \lambda_\theta^4 + \lambda_3^4 - 3\right), \tag{8}$$

where μ_1 and μ_2 represent coefficients of elasticity. In order to converge to the Hooke's law at small strains, the elastic coefficients should satisfy the identity $\mu = \mu_1 + 2\mu_2$, where μ is the elastic shear modulus measured for infinitesimal deformations. The principal components of the Cauchy stress tensor are

$$\sigma_i = \lambda_i\left(\frac{\partial \Psi}{\partial \lambda_i}\right) + p = \mu_1\lambda_i^2 + \mu_2\lambda_i^4 + p, \tag{9}$$

where $i \in \{s, \theta, 3\}$ correspond to the principal directions and p is the Lagrangian multiplier that represents the hydrostatic pressure. The unknown p is determined by balancing σ_3 with the Maxwell stress:

$$\sigma_M = -\varepsilon\frac{\Phi^2}{(\lambda_3 H)^2}, \tag{10}$$

where ε is the electrical permittivity, H is the natural thickness, and λ_3 is the transverse stretch [25]. Alternatively, the influence of applied voltage on mechanical deformation can be modeled by adding electrical enthalpy U_e to the potential energy functional. For a membrane with uniform electric field through its thickness, U_e can be computed by the following area integral in the current (deformed) placement:

$$U_e = \int_\Omega \Gamma \, d\Omega. \tag{11}$$

Here $\Gamma = -\varepsilon\Phi^2/2h^2$ is the electrical enthalpy density and can be added to Ψ to obtain a Lagrangian density for the potential energy functional Π.

2.3. Variational analysis

The total potential energy written w.r.t. the intermediate (prestretched) configuration Ω_p is expressed as:

$$\Pi = \int_{R_i}^{R_e} \mathcal{L}\, ds, \tag{12}$$

where the Lagrangian density $\mathcal{L} = 2\pi s h_p(\Psi + \Gamma)$ corresponds to the potential energy per unit width of each concentric ring forming the annulus. The explicit expression for $\mathcal{L}$ is obtained from Eqs. (6), (7), (8) and (11), and is reported in detail in Appendix A.1. At static equilibrium, Π must be minimized w.r.t. the functions $\{u_s, u_s', u_3'\}$, which implies the following stationary conditions (i.e. Euler–Lagrange equations):

$$\frac{\partial \mathcal{L}}{\partial u_s} - \frac{\partial}{\partial s}\frac{\partial \mathcal{L}}{\partial u_s'} = 0 \quad \text{and} \quad \frac{\partial}{\partial s}\frac{\partial \mathcal{L}}{\partial u_3'} = 0 \tag{13}$$

(see Appendix A.1 for the complete expressions). The solutions to the governing equations in (13) must satisfy the following set of boundary conditions:

$$u_s(s)|_{s=R_i} = 0 \qquad u_s(s)|_{s=R_e} = 0 \qquad u_3(s)|_{s=R_i} = \bar{u}$$
$$u_3(s)|_{s=R_e} = 0, \tag{14}$$

where $\bar{u}$ is the prescribed displacement of the inner shaft.

Once the solution to (13) with boundary conditions (14) is obtained, the out-of-plane stiffness K_3 of the device can be evaluated for different values of the applied voltage. This is done by applying *Castigliano's theorem* (or the *Crotti's theorem* in the generalized context of nonlinear elasticity) to establish a relationship between the shaft displacement $\bar{u}$ and the corresponding reaction force F. The force F is obtained from the following derivative of the total potential energy evaluated for the extremized potential $\Pi^* = \Pi(\mathbf{u}_0^*)$ at static equilibrium:

$$F = \frac{\partial \Pi^*}{\partial \bar{u}}. \tag{15}$$

Finally, the effective spring stiffness K_3 corresponds to the slope of the force–displacement curve at $\bar{u} = 0$:

$$K_3 = \left.\frac{\partial F}{\partial \bar{u}}\right|_{\bar{u}=0}. \tag{16}$$

It is worth noting that K_3 depends on the following set of parameters: $\{\lambda_p, \Phi, \mu_1, \mu_2, R_i, R_e\}$ so, at least in principle, it is possible to tune the stiffness of the device not only by varying prestretch, geometry and constitutive characteristics of the material, but also by exploiting the electromechanical coupling, i.e. by changing the drop voltage between the two sides of the membrane.

2.4. Approximate solution

In order to obtain a closed-form approximation that relates the out-of-plane stiffness K_3 and the voltage Φ, we use a *small-on-large* strategy. This is applicable by assuming that the displacements associated with the mapping $\chi_0 : \Omega_p \to \Omega$ are relatively small, thus employing a *first order incremental* approach. The kinematics introduced in the previous section is such that a further deformation is superimposed on the highly prestretched (intermediate) configuration Ω_p through the prescription of the displacement $\bar{u}$. Therefore, under the hypothesis that $\bar{u}$ is *relatively small*, and, consequently, the current configuration is not far from the intermediate configuration, a linear approximation of the kinematics can be used to predict incremental variations of the system response.

For sake of clarity, a displacement $\tilde{\mathbf{u}}_0$ can be defined by scaling $\mathbf{u}_0$ in (5) by a quantity $\eta \ll 1$, namely

$$\tilde{\mathbf{u}}_0 = \eta \mathbf{u}_0 = \eta\,(u_s \mathbf{e_s} + u_3 \mathbf{e_3})\,, \tag{17}$$

and used in place of $\mathbf{u}_0$ in the sequel. By performing a Taylor expansion of the Euler–Lagrange equations in (13) and keeping only first order terms w.r.t. η, one obtains a linearization for deformations from the intermediate configuration. Next, by substituting relation (17) in (A.1), Eq. (13) implies the following "scaled" set of Euler–Lagrangian equations:

$$u_s'' + \frac{1}{s}u_s' - \frac{1}{s^2}u_s = 0 \quad \text{and} \quad u_3'' + \frac{1}{s}u_3' = 0. \tag{18}$$

Note that, as expected in axisymmetric problems encountered in linear elasticity, the first order approximation of the problem does not depend on the constitutive behavior of the material when the boundary conditions are completely prescribed in terms of displacement.

As shown in (18) the system takes the form of a set of Euler–Cauchy differential equations that, with reference to boundary conditions in (14), leads to the following analytic solutions:

$$u_s(s) = 0 \quad \text{and} \quad u_3(s) = \frac{\log(s) - \log(R_e)}{\log(R_i) - \log(R_e)}\bar{u}. \tag{19}$$

The force in (15) can be thus expressed, after some algebraic manipulations, as follows:

$$F_l = 2\pi\varepsilon\Phi^2 \frac{\lambda_p^2}{H \log\left(\frac{R_i}{R_e}\right)}\bar{u} + g_F \tag{20}$$

where $g_F = g_F(\lambda_p, \bar{u}, \mu_1, \mu_2, R_i, R_e, H,)$ (see details in Appendix A.2) is a suitable function introduced – for the sake of simplicity – to highlight the 2nd-order dependence of F_l on the drop voltage Φ. Furthermore, an analytic scaled relationship among the out-of-plane stiffness at $\bar{u} = 0$, the drop voltage, the prestretch and the geometrical and constitutive parameters is obtained:

$$K_l = 2\pi\varepsilon\Phi^2 \frac{\lambda_p^2}{H \log\left(\frac{R_i}{R_e}\right)} + g_K, \tag{21}$$

where the function $g_K = \partial g_F/\partial \bar{u}|_{\bar{u}=0} = g_K(\lambda_p, \mu_1, \mu_2, R_i, R_e, H)$.

3. Results

The boundary value problem described by (13) and (14) is solved numerically using the *bvp4c* finite difference solver in MATLAB™ 2015b (The Mathworks, Inc.). The numerical plots of the full-nonlinear version and the analytic *linearized-scaled* version in (19) are obtained using Mathematica™ 10 (Wolfram Research, Inc.). Results are obtained for values of parameters presented in Table 1. These are based on values previously reported for the soft polyacrylate [30] (VHB 4910; 3M) used as the dielectric membrane and the device dimensions reported in [12]. It should be noted that there is significant variation in the stiffness of polyacrylate elastomers, which can have an elastic modulus ranging from ∼0.1 to 1 MPa [1,31,32]. Polydimethylsiloxane (PDMS) is another popular dielectric elastomer that exhibits a similar range of stiffness. This includes commercially available silicones like Sylgard 184 (Dow-Corning), Smooth-Sil 950 (Smooth-On), and EcoFlex 00-30 (Smooth-On), which were recently characterized for applications in soft-matter engineering by Case, White, & Kramer [33].

As with polyacrylate, silicone elastomers can be engineered to exhibit a variety of nonlinear stress–strain responses. This

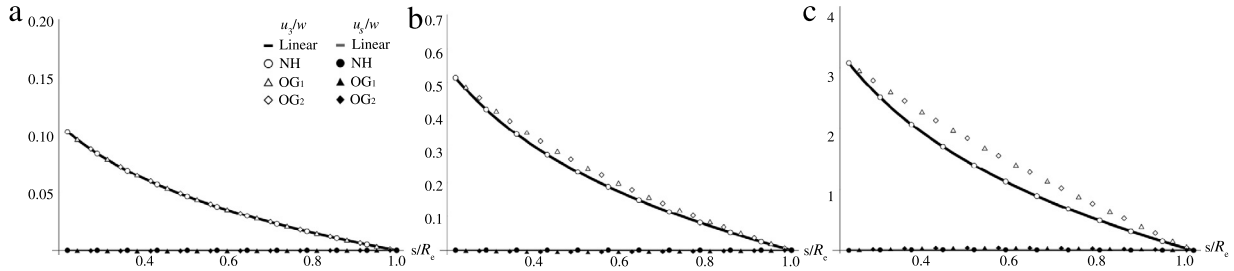

Fig. 2. Displacements u_3 and u_s, normalized w.r.t. the width of the annulus w, plotted versus the radial abscissa s normalized w.r.t. the external radius R_e, for values of the prescribed displacement $\bar{\mathbf{u}}$ equal to (a) 1 mm, (b) 5 mm, (c) 30 mm. The results are obtained for values of the parameters reported in Table 1, prestretch $\lambda_p = 6$ and applied drop voltage $\Phi = 1$ kV. For the constitutive model, the following three pairs of elastic coefficients were selected: (NH) $\mu_1 = \mu$ and $\mu_2 = 0$, which corresponds to a Neo-Hookean solid; (OG1) $\mu_1 = 0$ and $\mu_2 = \mu/2$; (OG2) $\mu_1 = \mu/2$ and $\mu_2 = \mu/4$.

Table 1
Parameters adopted in the simulations.

Physical parameter	Symbol	Value	Unit
Radius of shuttle	R_i	2.75	mm
Radius of circular frame	R_e	12.5	mm
Natural membrane thickness	H	1	mm
Elastic shear modulus [30]	μ	73	kPa
Relative permittivity	ε_r	3.21	–

ranges from the strain softening behavior consistent with a Neo-Hookean model to the stiffening or sequential softening–stiffening responses that can be captured by an Ogden model. To account for these different constitutive properties, we considered the following three pairs of elastic coefficients: (NH) $\mu_1 = \mu$ and $\mu_2 = 0$, which corresponds to a Neo-Hookean solid; (OG1) $\mu_1 = 0$ and $\mu_2 = \mu/2$; (OG2) $\mu_1 = \mu/2$ and $\mu_2 = \mu/4$.

In Fig. 2 the algebraic approximation (solid line) obtained from Eq. (19) is compared with the results of the numerical analysis (markers). The displacements $u_s = u_s(s)$ and $u_3 = u_3(s)$ are normalized w.r.t. the annular width $w = R_e - R_i$ and plotted against the normalized coordinate s/R_e for a prestretch $\lambda_p = 6$. The results of the nonlinear analyses are plotted for all the three constitutive models: NH (circle); OG1 (triangle); OG2 (rhombus). The plots have been obtained considering three different values of the external imposed displacement $\bar{u} = 1, 5, 30$ mm for sub-figures (a), (b), and (c), respectively, for a fixed drop voltage of $\Phi = 1$ kV. It is worth highlighting that the amplitude of the displacement u_s is always more than two orders of magnitude lower than the displacement u_3, as expected from the analytic solution in (19). As shown in Fig. A.9 in the Appendix A.3, in the case of a Neo-Hookean solid, this difference is even greater. Furthermore, the numerical solution for u_3 is close to the analytic solution if the amplitude of the imposed displacement is relatively low. Fig. 3 shows the normalized response force F/F_r versus displacement $\bar{u}/w$ for the analytic approximation (20) and numerical analysis performed on the three pairs of Ogden parameters. The force F_r is computed as the maximum force predicted by the analytic model at $\bar{u}/w = 0.5$: (NH; Fig. 3(a)) $F_r = 1.36$ N; (OG1; Fig. 3(b)) $F_r = 33.54$ N, (OG2; Fig. 3(c)) $F_r = 17.45$ N. Results are plotted for four different values of voltage ($\Phi = 0, 2, 4$ and 6 kV). As shown in Fig. 3 the analytic approximation from Eq. (20) is in very good agreement with the numerical solutions when $\bar{u}$ is relatively low. As $\bar{u}$ increases, some deviation is observed at higher displacements and voltages.

Next, Fig. 4 shows how the analytic solutions for the out-of-plane stiffness scale with voltage. Results are shown for the three constitutive models NH (Fig. 4(a)), OG1 (Fig. 4(b)), OG2 (Fig. 4(c)) in the limit as $\bar{u}$ goes to zero. The stiffness values are normalized to its K_0 evaluated when $\Phi = 0$ for each of the three selected prestretches: (NH) $K_0 = (302.93\ \text{N/m})(1 - \lambda_p^{-6})$; (OG1) $K_0 = (151.46\ \text{N/m})(\lambda_p^2 - \lambda_p^{-10})$; (OG2) $K_0 = (151.46\ \text{N/m})(1 - \lambda_p^{-6}) + (75.73\ \text{N/m})(\lambda_p^2 - \lambda_p^{-10})$. Consistently with the results in Fig. 3, significant voltage-induced softening response is only expected for the Neo-Hookean solid. For the other constitutive models, greater voltage or prestretch is required to observe a comparable stiffness change. This influence may be better examined by comparing the internal stress in the intermediate configuration in the radial direction.

Fig. 5 presents a combined plot of the radial stress normalized w.r.t. the membrane stress σ_0 at $\Phi = 0$ versus the applied voltage for the three constitutive models. In all cases, a prestretch of $\lambda_p = 6$ is selected and the corresponding membrane stresses are $\sigma_0 = 2.63$, 47.30, and 24.97 MPa for the NH, OG1, and OG2 solids, respectively. Although the prestretch induces different levels of residual stress, all the curves exhibit similar trends and profiles, i.e. $\sigma_s \propto -\Phi^2$. The key difference among the three cases is found as the voltage tends to a critical value (i.e. Φ^*) at which the stiffness approaches zero, that is: $\Phi^* \simeq 8$, 35, and 26 kV for the NH, OG1, and OG2 solids, respectively. It is important to note that, as shown in Fig. 5, not all the plotted values are physically realizable. This is due to dielectric breakdown, which occurs when the applied voltage exceeds the ability of the dielectric to hold charge and it is no longer an insulator. Fig. 6 contains an estimate of the voltages at which breakdown will occur for VHB 4910 (3M), which is a popular polyacrylate used in DE actuators and transducers [34] used in [12] to perform the experiment.

4. Discussion

As shown in Fig. 4, it is apparent that the mechanical impedance of the variable stiffness device is strongly affected by applied voltage, prestretch, and nonlinear constitutive properties of the dielectric. Even for materials exhibiting the same shear modulus at infinitesimal strain, high order strain softening or stiffening can lead to dramatic differences in the electromechanical response. This sensitivity arises from the fact that stiffness tuning is only pronounced when the electrostatic Maxwell stress is comparable to the residual membrane stress of the prestretched film. This is clear in Fig. 5, which shows that reduction is most pronounced when the value of the drop voltage induces a Maxwell stress with a magnitude compensating the amount of prestress (for larger voltages, the predicted stiffness is negative and likely corresponds to an electromechanical instability [13]).

In general, it is observed that for a Neo-Hookean solid, the analytic and numerical solutions are in very good agreement. In particular, the numerical solution for u_s is extremely small (except for $\bar{u} = 30$ mm) and there is virtually no discrepancy in the prediction for u_3. Even for the OG1 and OG2 solids, results from the analytic solution are found to be adequate to approximate the nonlinear profile of the membrane so long as the vertical displacement is moderate ($\bar{u} \leq 5$ mm).

In Fig. 3, it is evident that the out-of-plane response of the device to a pulling out displacement is strongly dependent on the

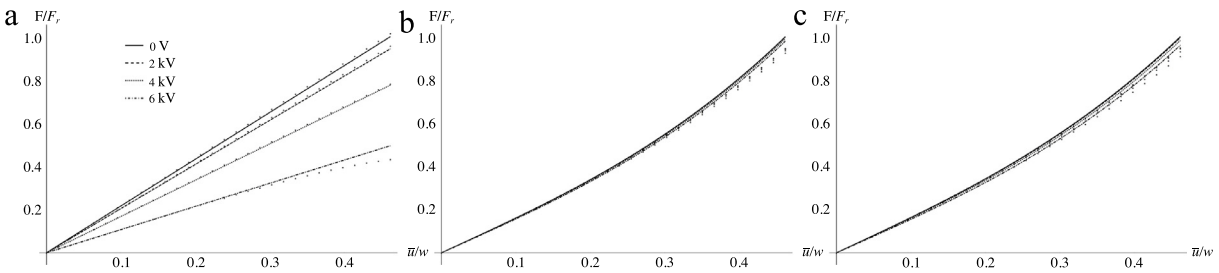

Fig. 3. Analytic (solid) and numeric (dotted) response force F normalized w.r.t. its maximum value versus the prescribed displacement $\bar{\mathbf{u}}$ normalized w.r.t. the annular width w, for different values of voltage ($\Phi = 0, 2, 4, 6$ kV) and for the three constitutive models: (a) NH ($\mu_1 = \mu$ and $\mu_2 = 0$); (b) OG1 ($\mu_1 = 0$ and $\mu_2 = \mu/2$); (c) OG2 ($\mu_1 = \mu/2$ and $\mu_2 = \mu/4$). The results are obtained for values of the parameters reported in Table 1 and prestretch $\lambda_p = 6$.

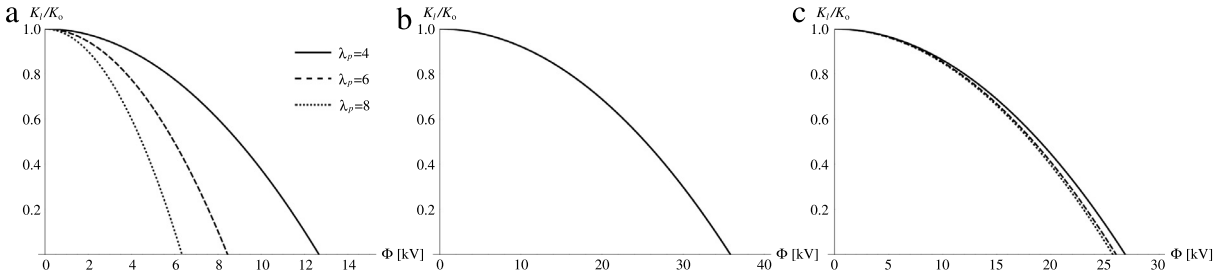

Fig. 4. Analytic prediction of the out-of-plane stiffness of the device K_l normalized w.r.t. its value K_0 evaluated for $\Phi = 0$ versus the applied voltage Φ for different values of prestretch ($\lambda_p = 4, 6, 8$), for different values of voltage ($\Phi = 0, 2, 4, 6$ kV) and for the three constitutive models: (a) NH ($\mu_1 = \mu$ and $\mu_2 = 0$) which corresponds to $K_0 = (302.93\ \text{N/m})(1 - \lambda_p^{-6})$; (b) OG1 ($\mu_1 = 0$ and $\mu_2 = \mu/2$) which corresponds to $K_0 = (151.46\ \text{N/m})(\lambda_p^2 - \lambda_p^{-10})$; (c) OG2 ($\mu_1 = \mu/2$ and $\mu_2 = \mu/4$) which corresponds to $K_0 = (151.46\ \text{N/m})(1 - \lambda_p^{-6}) + (75.73\ \text{N/m})(\lambda_p^2 - \lambda_p^{-10})$. The results are obtained for values of the parameters reported in Table 1.

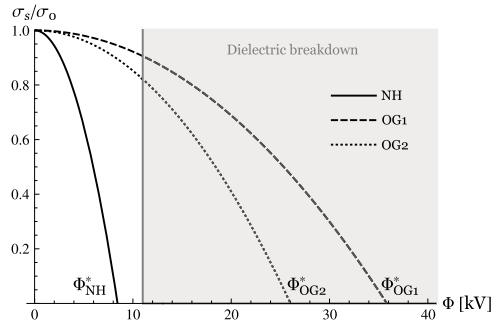

Fig. 5. Radial stress σ_s normalized w.r.t. the membrane stress σ_0 at $\Phi = 0$ versus the applied voltage for the three constitutive models: (a) NH ($\mu_1 = \mu$ and $\mu_2 = 0$) which corresponds to $\sigma_0 = 2.63$ MPa; (b) OG1 ($\mu_1 = 0$ and $\mu_2 = \mu/2$) which corresponds to $\sigma_0 = 47.30$ MPa; (c) OG2 ($\mu_1 = \mu/2$ and $\mu_2 = \mu/4$) which corresponds to 24.97 MPa, highlighting the region in which the dielectric breakdown occurs (gray region). The critical voltage Φ^*, at which the stress vanishes, is $\simeq 8, 35, 26$ kV for the NH, OG1, and OG2 model, respectively. The results are obtained for values of the parameters reported in Table 1 and prestretch $\lambda_p = 6$.

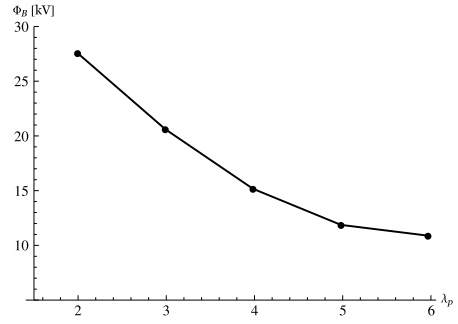

Fig. 6. Estimate of the breakdown voltage for the polyacrylate VHB 4910 (3M), for increasing value of prestretch λ_p, experimentally obtained by [34] when the elastomer sheet is bi-axially (pre)stretched.

constitutive behavior chosen to model the membrane. In the case of the Neo-Hookean solid, there is a pronounced *relaxing effect*, with a behavior comparable with the experiments by [12], that corresponds to a lower slope of the force–displacement curve with increasing voltage. It is important to note that this effect is not significant in the other two constitutive models. Such a difference illustrates the importance of performing an accurate experimental characterization of the polymer's constitutive properties. For the reader's convenience, force in Eq. (20) versus the normalized displacement of the device for the three constitutive models is presented in Fig. 7. This is displayed in comparison with the strain response in terms of first Piola–Kirchhoff stress normalized w.r.t. the tangent shear modulus versus stretch, in the case of uni-axial stress state. The presence of the parameter μ_2, as well known, induces a stiffening effect with an increase of the deformation that apparently interferes with the tunable stiffness coupling.

To examine how it might be possible to maximize the tuning effect, it is helpful to express Eq. (21) for the special case of a Neo-Hookean solid with $\bar{u} = 0$, namely:

$$K_{NH} = \frac{2\pi H}{\alpha}\left[\mu\left(1 - \frac{1}{\lambda_p^6}\right) - \varepsilon\Phi^2\frac{\lambda_p^2}{H^2}\right], \tag{22}$$

where $\alpha = \log(R_e/R_i)$. This shows in a simple way that the stiffness of the device corresponds to the difference in contributions from mechanical prestretch and electrical enthalpy. As shown in Fig. 8, prestretch can have an important role in the stiffness change. In fact, although there is a saturation effect in the first term with the brackets, a quadratic dependence in the second term with an increase of λ_p can be identified. A less pronounced (but non-negligible) effect can be related to a reduction of the initial thickness H and the reduction of the shear modulus of the membrane. As with λ_p, such parameters can be adjusted in order to influence electromechanical response.

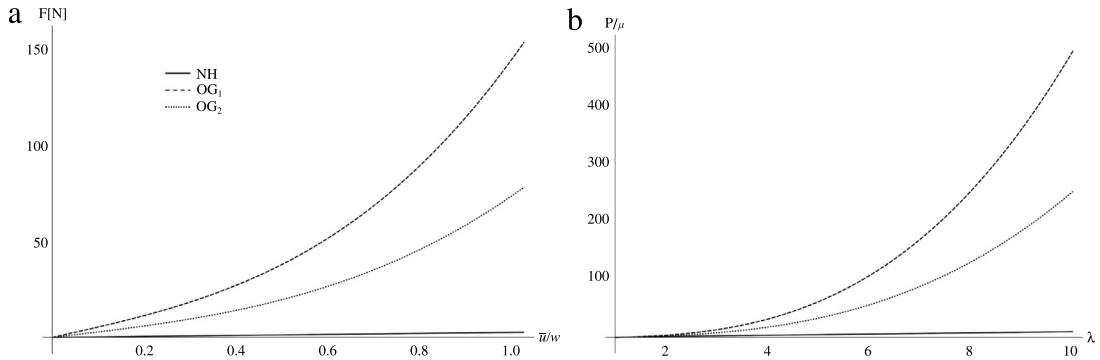

Fig. 7. Comparison between (a) the strain response of the device in terms of tensile force F versus the prescribed displacement $\bar{u}$ normalized w.r.t. the annular width w and (b) the strain response in terms of First Piola–Kirchhoff stress P normalized w.r.t. the tangent shear modulus (μ) versus stretch (λ) in a case of uni-axial stress state. The results are obtained for values of the parameters reported in Table 1, drop voltage $\Phi = 3$ kV and prestretch $\lambda_p = 6$. For the constitutive model, the following three pairs of elastic coefficients were selected: (NH) $\mu_1 = \mu$ and $\mu_2 = 0$, which corresponds to a Neo-Hookean solid; (OG1) $\mu_1 = 0$ and $\mu_2 = \mu/2$; (OG2) $\mu_1 = \mu/2$ and $\mu_2 = \mu/4$.

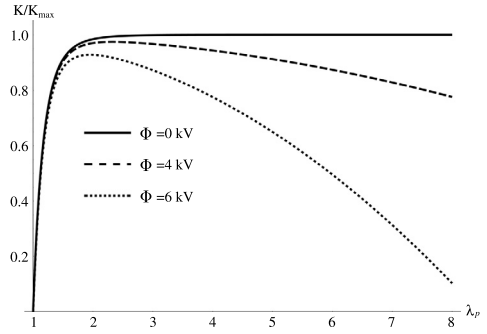

Fig. 8. Analytic stiffness response K specialized for the NH model, given by Eq. (22), normalized w.r.t. its value $K_{\max} \simeq 303$ N/m versus the prestretch λ_p, for different values of the applied voltage ($\Phi = 0, 4, 6$ kV). The results are obtained for values of the parameters reported in Table 1.

5. Conclusions

The variation of the out-of-plane stiffness of an annular DE membrane in response to an applied voltage has been analytically modeled. The theory takes into account the constitutive nonlinearity associated with large prestretch and electromechanical coupling from Maxwell stress. We show that the increase of voltage induces a nonlinear softening effect ($\propto -\Phi^2$) that is significantly more pronounced when the Maxwell stress is comparable to the amount of prestress. The analytic approximation of these values critically depends on the constitutive response of the membrane. This is due to the important role of the residual membrane stress when high prestretch λ_p is applied. Among the three models chosen to perform the simulation, for the cases of OG1 and OG2 a significant reduction of the stiffness occurs for voltages exceeding the experimentally estimated breakdown threshold. On the contrary, this is not the case for the NH solid and, thus, it is possible – at least in principle – to have a drastic reduction of the out-of-plane stiffness if the value of the imposed voltage is sufficiently close to a critical value Φ^*. This suggests that a membrane with constitutive properties similar to that of a Neo-Hookean solid behavior might allow for the largest changes in effective stiffness.

Acknowledgment

C.M. acknowledges support from the NASA Early Career Faculty Award (NNX14AO49G).

Appendix

A.1. Lagrangian

The energy density per unit length expressed in (12), considering the Eqs. (8) and (11) takes the form:

$$\begin{aligned}
&\mathcal{L}(u_s, u_s', u_3', s) \\
&= \frac{1}{2}\pi H s \left\{ - \frac{2\Phi^2 \varepsilon \lambda_p^4 (u_s+s)^2 \left[(u_s'+1)^2 + (u_3')^2 \right]}{H^2 s^2} \right. \\
&+ \mu_2 \left\{ \frac{s^4}{\lambda_p^8 (u_s+s)^4 \left[(u_s'+1)^2 + (u_3')^2 \right]^2} \right. \\
&\left. + \frac{\lambda_p^4 (u_s+s)^4}{s^4} + \lambda_p^4 \left[(u_s'+1)^2 + (u_3')^2 \right]^2 - 3 \right\} \\
&+ 2\mu_1 \left\{ 2\lambda_p^2 + \frac{s^2}{\lambda_p^4 (u_s+s)^2 \left[(u_s'+1)^2 + (u_3')^2 \right]} \right. \\
&\left. \left. + \frac{\lambda_p^2 u_s^2}{s^2} + \lambda_p^2 (u_s')^2 + \lambda_p^2 u_s' + 2\frac{2\lambda_p^2 u_s}{s} + \lambda_p^2 (u_3')^2 - 3 \right\} \right\} \quad \text{(A.1)}
\end{aligned}$$

To minimize $\mathcal{L}$, since it is function of (u_s, u_s', u_3), the following set of Euler–Lagrangian equations have to be imposed equal to zero:

$$\begin{aligned}
&\frac{\partial \mathcal{L}}{\partial u_s} - \frac{\partial}{\partial s}\frac{\partial \mathcal{L}}{\partial u_s'} \\
&= \frac{2\pi \varepsilon \Phi^2 (s+u_s) \left\{ s \left[-(u_3')^2 + (u_s')^2 + u_s' + s u_s'' \right] - u_s (u_s' - s u_s'' + 1) \right\} \lambda_p^2}{H s^2} \\
&+ \frac{H\pi}{2\lambda_p^2} \left\{ - \frac{4\mu_1 (u_s'+1) \left\{ \lambda_p^6 - \frac{s^2}{(s+u_s)^2 \left[(u_3')^2 + (u_s'+1)^2 \right]^2} \right\}}{\lambda_p^4} \right. \\
&\left. + s\mu_2 \left\{ \frac{4(s+u_s)^3 \lambda_p^4}{s^4} - \frac{4s^4}{(s+u_s)^5 \lambda_p^8 \left[(u_3')^2 + (u_s'+1)^2 \right]^2} \right\} \right.
\end{aligned}$$

$$
\begin{aligned}
&+\frac{4s\mu_1\left\{\frac{(s+u_s)^4\lambda_p^6}{s^2}-\frac{s^2\left(u_3'\right)^2}{\left[\left(u_3'\right)^2+\left(u_s'+1\right)^2\right]^2}-\frac{\left(u_s's+s\right)^2}{\left[\left(u_3'\right)^2+\left(u_s'+1\right)^2\right]^2}\right\}}{\left(s+u_s\right)^3\lambda_p^4}\\
&-\frac{4\mu_2\left(u_s'+1\right)\left\{\lambda_p^{12}\left[\left(u_3'\right)^2+\left(u_s'+1\right)^2\right]^4-\frac{s^4}{(s+u_s)^4}\right\}}{\lambda_p^8\left[\left(u_3'\right)^2+\left(u_s'+1\right)^2\right]^3}\\
&-\frac{4s\mu_1}{\lambda_p^4}\left\{u_s''\lambda_p^6-\frac{4s^2u_3'\left(u_s'+1\right)u_3''}{\left(s+u_s\right)^2\left[\left(u_3'\right)^2+\left(u_s'+1\right)^2\right]^3}\right.\\
&-\frac{2s^2\left(u_3'\right)^2u_s''}{\left(s+u_s\right)^2\left[\left(u_3'\right)^2+\left(u_s'+1\right)^2\right]^3}-\frac{2\left(u_s's+s\right)^2u_s''}{\left(s+u_s\right)^2\left[\left(u_3'\right)^2+\left(u_s'+1\right)^2\right]^3}\\
&+\frac{s\left(u_s'+su_s''+1\right)}{\left(s+u_s\right)^2\left[\left(u_3'\right)^2+\left(u_s'+1\right)^2\right]^2}-\frac{4s\left(u_s'+1\right)^2\left(u_s'+su_s''+1\right)}{\left(s+u_s\right)^2\left[\left(u_3'\right)^2+\left(u_s'+1\right)^2\right]^3}\\
&-\frac{4s^2\left(u_s'+1\right)\left[u_3'u_3''+\left(u_s'+1\right)u_s''\right]}{\left(s+u_s\right)^2\left[\left(u_3'\right)^2+\left(u_s'+1\right)^2\right]^3}\\
&+\frac{12s^2\left(u_s'+1\right)^3\left[u_3'u_3''+\left(u_s'+1\right)u_s''\right]}{\left(s+u_s\right)^2\left[\left(u_3'\right)^2+\left(u_s'+1\right)^2\right]^4}\\
&+\frac{12s^2\left(u_3'\right)^2\left(u_s'+1\right)\left[u_3'u_3''+\left(u_s'+1\right)u_s''\right]}{\left(s+u_s\right)^2\left[\left(u_3'\right)^2+\left(u_s'+1\right)^2\right]^4}\\
&-\frac{2s^2\left(u_s'+1\right)^2}{\left(s+u_s\right)^3\left[\left(u_3'\right)^2+\left(u_s'+1\right)^2\right]^2}+\frac{s\left(u_s'+1\right)}{\left(s+u_s\right)^2\left[\left(u_3'\right)^2+\left(u_s'+1\right)^2\right]^2}\\
&+\frac{4s^2\left(u_s'+1\right)^4}{\left(s+u_s\right)^3\left[\left(u_3'\right)^2+\left(u_s'+1\right)^2\right]^3}+\frac{4s^2\left(u_3'\right)^2\left(u_s'+1\right)^2}{\left(s+u_s\right)^3\left[\left(u_3'\right)^2+\left(u_s'+1\right)^2\right]^3}\\
&\left.-\frac{4s\left(u_3'\right)^2\left(u_s'+1\right)}{\left(s+u_s\right)^2\left[\left(u_3'\right)^2+\left(u_s'+1\right)^2\right]^3}\right\}-\frac{4s\mu_2}{\lambda_p^8}\left\{\left[\left(u_3'\right)^2+\left(u_s'+1\right)^2\right]u_s''\lambda_p^{12}\right.\\
&+\left(u_s'+1\right)\left[2u_3'u_3''+2\left(u_s'+1\right)u_s''\right]\lambda_p^{12}\\
&-\frac{s^4u_s''}{\left(s+u_s\right)^4\left[\left(u_3'\right)^2+\left(u_s'+1\right)^2\right]^3}+\frac{6s^4\left(u_s'+1\right)\left[u_3'u_3''+\left(u_s'+1\right)u_s''\right]}{\left(s+u_s\right)^4\left[\left(u_3'\right)^2+\left(u_s'+1\right)^2\right]^4}\\
&\left.\left.+\frac{4s^4\left(u_s'+1\right)^2}{\left(s+u_s\right)^5\left[\left(u_3'\right)^2+\left(u_s'+1\right)^2\right]^3}-\frac{4s^3\left(u_s'+1\right)}{\left(s+u_s\right)^4\left[\left(u_3'\right)^2+\left(u_s'+1\right)^2\right]^3}\right\}\right\}
\end{aligned}
\tag{A.2}
$$

and

$$
\begin{aligned}
\frac{\partial}{\partial s}\frac{\partial\mathcal{L}}{\partial u_3'}=&-\frac{2\pi\epsilon\Phi^2\left(s+u_s\right)\lambda_p^2\left[u_3'\left(2u_s's+s-u_s\right)+s\left(s+u_s\right)u_3''\right]}{Hs^2}\\
&+\frac{2H\pi}{\lambda_p^{10}}\left\{\mu_1u_3'\left\{\lambda_p^6-\frac{s^2}{\left(s+u_s\right)^2\left[\left(u_3'\right)^2+\left(u_s'+1\right)^2\right]^2}\right\}\lambda_p^4\right.\\
&+s\mu_1\lambda_p^4\left\{u_3''\lambda_p^6+\frac{s^2u_3''}{\left(s+u_s\right)^2\left[\left(u_3'\right)^2+\left(u_s'+1\right)^2\right]^2}\right.\\
&-\frac{6s^2\left(u_3'\right)^2u_3''}{\left(s+u_s\right)^2\left[\left(u_3'\right)^2+\left(u_s'+1\right)^2\right]^3}-\frac{2\left(u_s's+s\right)^2u_3''}{\left(s+u_s\right)^2\left[\left(u_3'\right)^2+\left(u_s'+1\right)^2\right]^3}\\
&-\frac{4su_3'\left(u_s'+1\right)\left(u_s'+su_s''+1\right)}{\left(s+u_s\right)^2\left[\left(u_3'\right)^2+\left(u_s'+1\right)^2\right]^3}-\frac{4s^2u_3'\left[u_3'u_3''+\left(u_s'+1\right)u_s''\right]}{\left(s+u_s\right)^2\left[\left(u_3'\right)^2+\left(u_s'+1\right)^2\right]^3}\\
&+\frac{12s^2\left(u_3'\right)^3\left[u_3'u_3''+\left(u_s'+1\right)u_s''\right]}{\left(s+u_s\right)^2\left[\left(u_3'\right)^2+\left(u_s'+1\right)^2\right]^4}\\
&+\frac{6u_3'\left(u_s's+s\right)^2\left[2u_3'u_3''+2\left(u_s'+1\right)u_s''\right]}{\left(s+u_s\right)^2\left[\left(u_3'\right)^2+\left(u_s'+1\right)^2\right]^4}\\
&+\frac{2su_3'}{\left(s+u_s\right)^2\left[\left(u_3'\right)^2+\left(u_s'+1\right)^2\right]^2}-\frac{2s^2u_3'\left(u_s'+1\right)}{\left(s+u_s\right)^3\left[\left(u_3'\right)^2+\left(u_s'+1\right)^2\right]^2}\\
&-\frac{4s\left(u_3'\right)^3}{\left(s+u_s\right)^2\left[\left(u_3'\right)^2+\left(u_s'+1\right)^2\right]^3}\\
&+\frac{4s^2u_3'\left(u_s'+1\right)^3}{\left(s+u_s\right)^3\left[\left(u_3'\right)^2+\left(u_s'+1\right)^2\right]^3}\\
&\left.+\frac{4s^2\left(u_3'\right)^3\left(u_s'+1\right)}{\left(s+u_s\right)^3\left[\left(u_3'\right)^2+\left(u_s'+1\right)^2\right]^3}\right\}\\
&+\frac{\mu_2u_3'\left\{\lambda_p^{12}\left[\left(u_3'\right)^2+\left(u_s'+1\right)^2\right]^4-\frac{s^4}{(s+u_s)^4}\right\}}{\left[\left(u_3'\right)^2+\left(u_s'+1\right)^2\right]^3}\\
&+s\mu_2\left\{\left[\left(u_3'\right)^2+\left(u_s'+1\right)^2\right]u_3''\lambda_p^{12}+u_3'\left[2u_3'u_3''+2\left(u_s'+1\right)u_s''\right]\lambda_p^{12}\right.\\
&-\frac{s^4u_3''}{\left(s+u_s\right)^4\left[\left(u_3'\right)^2+\left(u_s'+1\right)^2\right]^3}+\frac{6s^4u_3'\left[u_3'u_3''+\left(u_s'+1\right)u_s''\right]}{\left(s+u_s\right)^4\left[\left(u_3'\right)^2+\left(u_s'+1\right)^2\right]^4}\\
&-\frac{4s^3u_3'}{\left(s+u_s\right)^4\left[\left(u_3'\right)^2+\left(u_s'+1\right)^2\right]^3}\\
&\left.\left.+\frac{4s^4u_3'\left(u_s'+1\right)}{\left(s+u_s\right)^5\left[\left(u_3'\right)^2+\left(u_s'+1\right)^2\right]^3}\right\}\right\}.
\end{aligned}
\tag{A.3}
$$

A.2. g_F

The function $g_F(\lambda_p, \bar{u}, \mu_1, \mu_2, R_1, R_2, H,)$ introduced in Eq. (20) for sake of clarity in order to isolate the dependence of the force on the drop voltage takes the form:

$$
\begin{aligned}
g_F=&\frac{H\pi\bar{u}}{2\alpha^4\left(\bar{u}^2+\alpha^2R_e^2\right)^2\left(\bar{u}^2+\alpha^2R_i^2\right)^2\lambda_p^{10}}\\
&\times\left\{2\left\{-\log\left(\bar{u}^2+\alpha^2R_e^2\right)\left[\bar{u}^4R_e^4+\bar{u}^2\left(\bar{u}^2+2\alpha^2R_e^2\right)R_i^2R_e^2\right.\right.\right.\\
&\left.+\left(\bar{u}^2+\alpha^2R_e^2\right)^2R_i^4\right]\mu_2\alpha^4+\log\left(\bar{u}^2+\alpha^2R_i^2\right)\\
&\times\left[\bar{u}^4R_e^4+\bar{u}^2\left(\bar{u}^2+2\alpha^2R_e^2\right)R_i^2R_e^2\right.\\
&\left.+\left(\bar{u}^2+\alpha^2R_e^2\right)^2R_i^4\right]\mu_2\alpha^4\\
&-\log\left(\frac{\bar{u}^2+\alpha^2R_e^2}{\bar{u}^2+\alpha^2R_i^2}\right)\left(\bar{u}^2+\alpha^2R_e^2\right)^2\left(\bar{u}^2+\alpha^2R_i^2\right)^2\lambda_p^4\mu_1\\
&+\log\left(\frac{\bar{u}^2+\alpha^2R_i^2}{\bar{u}^2+\alpha^2R_e^2}\right)\bar{u}^4\left[3R_e^2R_i^2\alpha^4\right.
\end{aligned}
$$

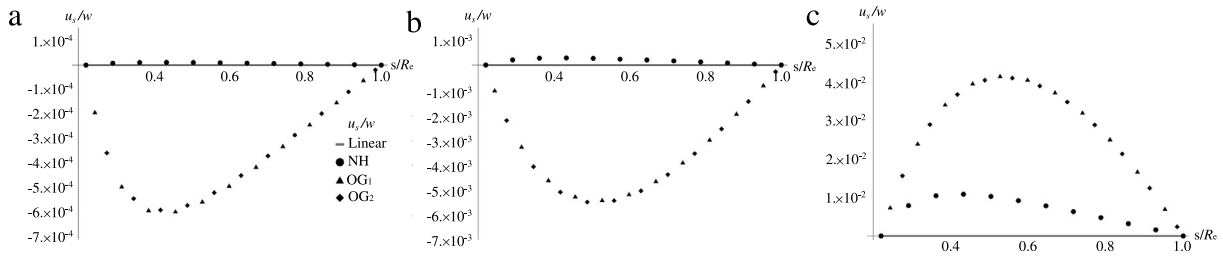

Fig. A.9. Displacements u_s, normalized w.r.t. the width of the annulus w, plotted versus the radial abscissa s normalized w.r.t. the external radius R_e, for values of the prescribed displacement $\bar{\mathbf{u}}$ equal to (a) 1 mm, (b) 5 mm, (c) 30 mm. The results are obtained for values of the parameters reported in Table 1, prestretch $\lambda_p = 6$ and applied drop voltage $\Phi = 1$ kV. For the constitutive model, the following three pairs of elastic coefficients were selected: (NH) $\mu_1 = \mu$ and $\mu_2 = 0$, which corresponds to a Neo-Hookean solid; (OG1) $\mu_1 = 0$ and $\mu_2 = \mu/2$; (OG2) $\mu_1 = \mu/2$ and $\mu_2 = \mu/4$.

$$
\begin{aligned}
&+ 2\bar{u}^2\left(R_e^2 + R_i^2\right)\alpha^2 + \bar{u}^4\Big]\mu_2\Big\}\alpha^2 \\
&+ \frac{1}{R_e^2 R_i^2}\Big\{2\bar{u}^6 R_e^2\left(\bar{u}^2 + \alpha^2 R_e^2\right)^2\mu_2\lambda_p^{12} \\
&+ \alpha^4 R_i^6\Big\{2\alpha^2 R_e^2\left(\bar{u}^2 + \alpha^2 R_e^2\right) \\
&\times\left[2\alpha\left(\bar{u}^2 + \alpha^2 R_e^2\right)\lambda_p^6 - \bar{u}^2\right]\mu_1\lambda_p^4 \\
&+ \Big[-2\left(\bar{u}^2 + \alpha^2 R_e^2\right)^2\left(\bar{u}^2 - 2\alpha^3 R_e^2\right)\lambda_p^{12} \\
&- 4\alpha^4\bar{u}^2 R_e^4 - 3\alpha^2\bar{u}^4 R_e^2\Big]\mu_2\Big\} \\
&+ \bar{u}^4 R_i^2\Big\{2\alpha^3 R_e^2\left(\bar{u}^2 + \alpha^2 R_e^2\right) \\
&\times\left[2\bar{u}^2\lambda_p^6 + \alpha R_e^2\left(2\alpha\lambda_p^6 + 1\right)\right]\mu_1\lambda_p^4 \\
&+ \Big\{-2\left(\bar{u}^2 + \alpha^2 R_e^2\right)^2\left[\bar{u}^2 - 2\alpha^2(\alpha+1)R_e^2\right] \\
&\times\lambda_p^{12} + 3\alpha^6 R_e^6 + 2\alpha^4\bar{u}^2 R_e^4\Big\}\mu_2\Big\} \\
&+ 2\alpha^2\bar{u}^2 R_i^4\Big\{\alpha^2 R_e^2\Big[4\alpha\left(\bar{u}^2 + \alpha^2 R_e^2\right)^2\lambda_p^6 - \bar{u}^4 + \alpha^4 R_e^4\Big] \\
&\times\mu_1\lambda_p^4 + \Big\{\left(\bar{u}^2 + \alpha^2 R_e^2\right)^2\left[\alpha^2(4\alpha+1)R_e^2 - 2\bar{u}^2\right] \\
&\times\lambda_p^{12} + 2\alpha^6 R_e^6 - \alpha^2\bar{u}^4 R_e^2\Big\}\mu_2\Big\}\Big\}\Big\}. \qquad \text{(A.4)}
\end{aligned}
$$

A.3. u_s

The component of the displacement in the s-direction is here shown in Fig. A.9.

References

[1] W. Shan, T. Lu, C. Majidi, Soft-matter composites with electrically tunable elastic rigidity, Smart Mater. Struct. 22 (8) (2013) 085005.

[2] B.E. Schubert, D. Floreano, Variable stiffness material based on rigid low-melting-point-alloy microstructures embedded in soft poly (dimethylsiloxane)(pdms), RSC Adv. 3 (46) (2013) 24671–24679.

[3] F. Gandhi, S.-G. Kang, Beams with controllable flexural stiffness, Smart Mater. Struct. 16 (4) (2007) 1179–1184.

[4] G. Mcknight, R. Doty, A. Keefe, G. Herrera, C. Henry, Segmented reinforcement variable stiffness materials for reconfigurable surfaces, J. Intell. Mater. Syst. Struct. 21 (17) (2010) 1783–1793.

[5] W. Shan, S. Diller, A. Tutcuoglu, C. Majidi, Rigidity-tuning conductive elastomer, Smart Mater. Struct. 24 (6) (2015) 065001. URL http://dx.doi.org/10.1088/0964-1726/24/6/065001.

[6] Y. Bar-Cohen, Electroactive Polymer (EAP) Actuators as Artificial Muscles: Reality, Potential, and Challenges, second ed., SPIEThe International Society for Optical Engineering, USA, 2004.

[7] Y. Bar-Cohen, Electroactive polymers as an enabling materials technology, Proc. Inst. Mech. Eng. Part G: J. Aerospace Eng. 221 (4) (2007) 553–564.

[8] O.A. Araromi, I. Gavrilovich, J. Shintake, S. Rosset, M. Richard, V. Gass, H.R. Shea, Rollable multisegment dielectric elastomer minimum energy structures for a deployable microsatellite gripper, IEEE/ASME Trans. Mechatronics 20 (1) (2015) 438–446.

[9] F. Carpi, D.D. Rossi, R. Kornbluh, R. Pelrine, P. Sommer-Larsen, Dielectric Elastomers as Electromechanical Transducer, 2007, p. 329.

[10] R. Pelrine, R. Kornbluh, Variable-Stiffness Mode Dielectric Elastomer Devices, 61, 2008, 192–201. http://dx.doi.org/10.4028/www.scientific.net/AST.61.192.

[11] F. Carpi, G. Frediani, C. Gerboni, J. Gemignani, D. De Rossi, Enabling variable-stiffness hand rehabilitation orthoses with dielectric elastomer transducers, Med. Eng. Phys. 36 (2) (2014) 205–211. URL http://dx.doi.org/10.1016/j.medengphy.2013.10.015, http://linkinghub.elsevier.com/retrieve/pii/S1350453313002361.

[12] S. Dastoor, M. Cutkosky, Design of dielectric electroactive polymers for a compact and scalable variable stiffness device, in: 2012 IEEE International Conference on Robotics and Automation, IEEE, 2012, pp. 3745–3750. http://dx.doi.org/10.1109/ICRA.2012.6224808, no. April. URL http://ieeexplore.ieee.org/lpdocs/epic03/wrapper.htm?arnumber=6224808.

[13] F. Yang, Electromechanical instability of microscale structures, J. Appl. Phys. 92 (5) (2002) 2789. URL http://scitation.aip.org/content/aip/journal/jap/92/5/10.1063/1.1496123.

[14] A. Orita, M.R. Cutkosky, Scalable Electroactive Polymer for Variable Stiffness Suspensions, IEEE/ASME Trans. Mechatronics 21 (6) (2016) 2836–2846. http://dx.doi.org/10.1109/TMECH.2016.2586484, URL http://ieeexplore.ieee.org/document/7501803/.

[15] Zhihang Ye, Zheng Chen, Ka Wai Kong, H. Chan, Robust control of dielectric elastomer diaphragm actuator for replicating human pulse, in: 2016 IEEE International Conference on Automation Science and Engineering, (CASE), IEEE, 2016, pp. 188–193. http://dx.doi.org/10.1109/COASE.2016.7743379, URL http://ieeexplore.ieee.org/document/7743379/.

[16] Z. Lu, Y. Cui, M. Debiasi, Active membrane-based silencer and its acoustic characteristics, Appl. Acoust. 111 (2016) 39–48. URL http://dx.doi.org/10.1016/j.apacoust.2016.03.042.

[17] K. Jia, M. Wang, T. Lu, J. Zhang, T. Wang, Band-gap tunable dielectric elastomer filter for low frequency noise, Smart Mater. Struct. 25 (5) (2016) 055047. http://dx.doi.org/10.1088/0964-1726/25/5/055047, URL http://stacks.iop.org/0964-1726/25/i=5/a=055047?key=crossref.0d081d3a2d56f136938b20caa0a2de11.

[18] T. He, X. Zhao, Z. Suo, Dielectric elastomer membranes undergoing inhomogeneous deformation, J. Appl. Phys. 106 (8) (2009) 083522. URL http://aip.scitation.org/doi/10.1063/1.3253322.

[19] A. Melnikov, R.W. Ogden, Finite deformations of an electroelastic circular cylindrical tube, Z. Angew. Math. Phys. 67 (6) (2016). http://dx.doi.org/10.1007/s00033-016-0733-0.

[20] C. Majidi, R.E. Groff, R.S. Fearing, Analysis of Shaft-Loaded Membrane Delamination Using Stationary Principles, Math. Mech. Solids 13 (1) (2007) 3–22. URL http://mms.sagepub.com/cgi/doi/10.1177/1081286506068823.

[21] K.-T. Wan, D.A. Dillard, Adhesion of a flat punch adhered to a thin pre-stressed membrane, J. Adhes. 79 (2) (2003) 123–140.

[22] R. Pelrine, R. Kornbluh, Q. Pei, J. Joseph, High-speed electrically actuated elastomers with strain greater than 100%, Science 287 (5454) (2000) 836–839.

[23] G. Kofod, P. Sommer-Larsen, R. Kornbluh, R. Pelrine, Actuation Response of Polyacrylate Dielectric Elastomers, J. Intell. Mater. Syst. Struct. 14 (12) (2003) 787–793. http://dx.doi.org/10.1177/1045389X03039260.

[24] R.M. McMeeking, C.M. Landis, Electrostatic forces and stored energy for deformable dielectric materials, J. Appl. Mech. 72 (4) (2005) 581–590.

[25] Z. Suo, X. Zhao, W.H. Greene, A nonlinear field theory of deformable dielectrics, J. Mech. Phys. Solids 56 (2) (2008) 467–486.

[26] J. Biggs, K. Danielmeier, J. Hitzbleck, J. Krause, T. Kridl, S. Nowak, E. Orselli, X. Quan, D. Schapeler, W. Sutherland, J. Wagner, Electroactive polymers: Developments of and perspectives for dielectric elastomers, Angew. Chem. Int. Ed. 52 (36) (2013) 9409–9421. http://dx.doi.org/10.1002/anie.201301918.

[27] L. Romasanta, M. Lopez-Manchado, R. Verdejo, Increasing the performance of dielectric elastomer actuators: A review from the materials perspective, Prog. Polym. Sci. 51 (2015) 188–211. URL http://dx.doi.org/10.1016/j.progpolymsci.2015.08.002.

[28] M.E. Gurtin, E. Fried, L. Anand, The Mechanics and Thermodynamics of Continua, Cambridge University Press, Cambridge, 2010, http://dx.doi.org/10.1017/CBO9780511762956, URL http://ebooks.cambridge.org/ref/id/CBO9780511762956.

[29] G.A. Holzapfel, Nonlinear Solid Mechanics: A Continuum Approach for Engineering, John Wiley & Sons, 2000.

[30] M. Bozlar, C. Punckt, S. Korkut, J. Zhu, C. Chiang Foo, Z. Suo, I.A. Aksay, Dielectric elastomer actuators with elastomeric electrodes, Appl. Phys. Lett. 101 (9) (2012). http://dx.doi.org/10.1063/1.4748114.

[31] S. Michel, X.Q. Zhang, M. Wissler, C. Löwe, G. Kovacs, A comparison between silicone and acrylic elastomers as dielectric materials in electroactive polymer actuators, Polym. Int. 59 (3) (2010) 391–399.

[32] S.M. Ha, W. Yuan, Q. Pei, R. Pelrine, S. Stanford, Interpenetrating polymer networks for high-performance electroelastomer artificial muscles, Adv. Mater. 18 (7) (2006) 887–891.

[33] J.C. Case, E.L. White, R.K. Kramer, Soft material characterization for robotic applications, Soft Robotics 2 (2) (2015) 80–87.

[34] J. Huang, S. Shian, R.M. Diebold, Z. Suo, D.R. Clarke, The thickness and stretch dependence of the electrical breakdown strength of an acrylic dielectric elastomer, Appl. Phys. Lett. 101 (12) (2012) 122905. URL http://scitation.aip.org/content/aip/journal/apl/101/12/10.1063/1.4754549.